

Pattern selection in the absolutely unstable regime as a nonlinear eigenvalue problem: Taylor vortices in axial flow

P. Büchel, M. Lücke, D. Roth

Institut für Theoretische Physik, Universität des Saarlandes, D-66041 Saarbrücken, Germany

R. Schmitz

Institut für Festkörperforschung, Forschungszentrum, D-52425 Jülich, Germany

Abstract

A unique pattern selection in the absolutely unstable regime of a driven, nonlinear, open-flow system is analyzed: The spatiotemporal structures of rotationally symmetric vortices that propagate downstream in the annulus of the rotating Taylor-Couette system due to an externally imposed axial through-flow are investigated for two different axial boundary conditions at the in- and outlet. Detailed quantitative results for the oscillation frequency, the axial profile of the wave number, and the temporal Fourier amplitudes of the propagating vortex patterns obtained by numerical simulations of the Navier-Stokes equations are compared with results of the appropriate Ginzburg-Landau amplitude equation approximation and also with experiments. Unlike the stationary patterns in systems without through-flow the spatiotemporal structures of propagating vortices are independent of parameter history, initial conditions, and system's length. They do, however, depend on the axial boundary conditions in addition to the driving rate of the inner cylinder and the through-flow rate. Our analysis of the amplitude equation shows that the pattern selection can be described by a nonlinear eigenvalue

problem with the frequency being the eigenvalue. The complex amplitude being the corresponding eigenfunction describes the axial structure of intensity and wave number. Small, but characteristic differences in the structural dynamics between the Navier-Stokes equations and the amplitude equation are mainly due to the different dispersion relations. Approaching the border between absolute and convective instability the eigenvalue problem becomes effectively linear and the selection mechanism approaches that one of linear front propagation.

47.54.+r,47.20.Ky,47.32.-y,47.20.Ft

I. INTRODUCTION

In many nonlinear continuous systems dissipative structures branch out of a homogeneous basic state when the external stress exceeds a critical threshold. Examples for these transitions are Taylor-Couette flow, Rayleigh-Bénard convection, binary-fluid convection, flame-front propagation, and some chemical or biological processes [1]. Often, for a fixed configuration of parameters and boundary conditions a continuous or discrete family of patterns with different wave numbers is stable. Their stability regime, e. g., a band of wave numbers might be limited by the possibility of resonant triad interactions of modes like those described by the Eckhaus or Benjamin-Feir mechanism [1]. The stable structures within such a band can be generated by appropriately engineered time histories of the parameters and/or by properly changing the boundary conditions, e. g., the system size. The most intensively investigated examples in this respect are the structures of Taylor vortices [1–7] in an annulus between concentric cylinders of which the inner one rotates and convective roll patterns in horizontal layers of one-component fluids [1,8–11,5] or binary mixtures heated from below [12,13].

This multiplicity of solutions of the underlying nonlinear partial differential equations that stably coexist for a fixed configuration of parameters and boundary conditions seems to disappear in an open-flow system: Recent numerical simulations of Rayleigh-Bénard convective rolls traveling downstream in an imposed horizontal Poiseuille flow showed [14–16] that their structure is uniquely selected – i. e. it is independent of parameter history, initial conditions, and system size – in the absolutely unstable regime. This is the parameter regime of an open-flow system in which the secondary pattern starting, e. g., from a spatially localized perturbation can grow in upstream as well as in downstream direction [17]. By contrast, in the convectively unstable regime [18] initial perturbations are blown out of the system – both, the upstream as well as the downstream facing front of the growing structure move downstream. In the absolutely unstable regime the structure expansion proceeds until the upstream (downstream) moving front encounters in a finite system the

inlet (outlet) and adjusts to the inlet (outlet) boundary condition. The final pattern resulting in such a situation shows a characteristic streamwise profile of the amplitude growing with increasing distance from the inlet and of the wave number variation, and a characteristic global oscillation frequency associated with the downstream motion of the pattern.

In this work we elucidate in numerical and analytical detail how such a uniquely selected spatiotemporal pattern structure can be understood as a nonlinear eigenvalue problem with the oscillation frequency being the eigenvalue and the profiles of pattern intensity and wave number determining the corresponding eigenfunction. We also show how this pattern selection process is related to the one occurring behind a front or "domain wall" that spatially separates an unstable, homogeneous state from a stable, structured state. To that end we present results of extensive numerical and analytical investigations of vortex patterns in the annulus of the Taylor-Couette setup with an externally imposed axial through-flow. For small through-flow rates and small rotation rates of the inner cylinder the structure of propagating vortex (PV) flow with vortices being advected in downstream direction is rotationally symmetric. Only for higher through-flow rates, which are not investigated here, there is a bifurcation [19,20] to spirals [20–26]. We have performed numerical simulations of the full, rotationally symmetric, two dimensional (2D) Navier-Stokes equations (NSE). They are compared with our numerical and analytical results obtained from the appropriate [27] 1D Ginzburg-Landau amplitude equation (GLE) approximation to the problem of PV flow and with experimental results [20–22,25,28,29]

The eigenvalue problem of the pattern selection by the imposed flow can best be analyzed and explained within the GLE framework. Therein, the complex amplitude $A(z, t)$ of the PV flow depends in the absolutely unstable regime on the streamwise position z and on time t in a multiplicative way only,

$$A(z, t) = a(z)e^{-i\Omega t}, \quad (1.1)$$

after transients have died out. The z -independent frequency Ω and the complex, z -dependent amplitude $a(z)$ that describes the streamwise variation of pattern modulus and wave number

are simultaneously fixed via a solvability condition in the form of a nonlinear eigenvalue problem. The selection of Ω and $a(z)$ seems to result from requiring the spatial variation of the amplitude to be as small as possible under the imposed boundary conditions for A at the ends of the annulus.

Approaching the border between the absolutely and convectively unstable regimes the pattern selection mechanism becomes linear: For driving and through-flow rates on this border line the selected frequency is the one resulting from a linear front whose spatiotemporal behavior is governed by the fastest growing linear mode. The latter is identified by a particular saddle of the complex linear dispersion relation over the complex wave number plane [1]. Now, the linear dispersion relations of NSE [30] and GLE differ for supercritical control parameters. And therefore the PV structures selected by NSE or GLE differ in a characteristic way.

It should be emphasized that the structural dynamics of pattern formation in the convectively unstable regime at larger through-flow rates and/or smaller driving rates substantially differs from the one investigated here in the absolutely unstable regime. The latter regime is governed by nonlinear contributions in the balance equations; the resulting patterns are uniquely selected and insensitive to initial conditions, parameter history, and small perturbations. On the other hand, in the convectively unstable regime that has attracted more experimental activities lately [28,29,31–35] the growing patterns are sensitive to initial conditions and perturbations. Thus, e. g., the noise sustained patterns [36] occurring in this regime depend on details of the spatiotemporal properties of the perturbation source.

The Taylor-Couette system [37] with an imposed axial through-flow has been investigated as a well defined open-flow system theoretically [38] and experimentally [39] since the beginning 1930s. Linear stability analyses of the basic state to traveling axisymmetric vortices were performed using various approximations, e. g. , for the narrow-gap limit, or simplified azimuthal velocity, or axial through-flow profiles [40], and later on for various aspect ratios fixed by the diameters of both cylinders [19,20,41,42]. Also, many experiments and comparisons with the theoretical predictions were done [21–25,28,29,31–35,43,44].

Our paper is organized as follows: In Sec. II we describe the system, the subregions of absolute and convective instability, and our methods of investigation. Furthermore, we recapitulate the GLE. The next section presents the spatiotemporal behavior of PV patterns obtained numerically for two different boundary conditions. In Sec. IV we analytically and numerically elucidate the pattern selection observed within the GLE and the NSE. We compare the results with each other, with front propagation, and with experiments. The last section gives a conclusion.

II. THE SYSTEM

We investigate time-dependent, rotationally symmetric vortex structures in a Taylor-Couette apparatus with an externally enforced axial flow. The viscous, incompressible fluid is confined to the annulus between two concentric cylinders of inner radius r_1 and outer radius r_2 . The setup is characterized by two geometric parameters: the radius ratio $\eta = \frac{r_1}{r_2}$ and the aspect ratio Γ , i.e., the quotient of the axial extension of the annulus and the gap width $d = r_2 - r_1$. Mostly we have used in our numerical simulations an aspect ratio of $\Gamma = 50$ and a radius ratio of $\eta = 0.75$. The outer cylinder is always kept at rest, while the inner one has a rotation rate Ω_{cyl} . In addition we impose a small through-flow in axial direction. The boundary conditions at r_1 and r_2 were always no slip. The conditions at the two ends $z = 0$ and $z = \Gamma$ of the annulus are explained in Sec. III.

The flow pattern is described by the momentum balance equation for the velocity field \mathbf{u} , the Navier-Stokes equations

$$(\partial_t + \mathbf{u} \cdot \nabla) \mathbf{u} = -\frac{1}{\varrho} \nabla p + \nu \nabla^2 \mathbf{u}, \quad (2.1a)$$

and the continuity equation

$$\nabla \cdot \mathbf{u} = 0 \quad (2.1b)$$

which reflects the incompressibility of the fluid. Here ν is the kinematic viscosity, ϱ the

mass density, and p the pressure. The system is characterized by two dimensionless control parameters. The Taylor number

$$T = \frac{\eta}{1-\eta} \frac{\Omega_{cyl}^2 d^4}{\nu^2} \quad (2.2)$$

is given by the squared rotation rate Ω_{cyl} of the inner cylinder. The Reynolds number

$$Re = \frac{\bar{w} d}{\nu} \quad (2.3)$$

is proportional to the mean axial through-flow velocity \bar{w} . For an axially uniform system the homogeneous basic flow state [45]

$$\mathbf{U}(r) = V_{CCF}(r) \mathbf{e}_\varphi + W_{APF}(r) \mathbf{e}_z \quad (2.4)$$

is a linear superposition of circular Couette flow (CCF)

$$V_{CCF}(r) = Ar + \frac{B}{r} \quad (2.5)$$

in azimuthal direction and of annular Poiseuille flow (APF)

$$W_{APF}(r) = \frac{r^2 + C \ln r + D}{E} Re \quad (2.6)$$

in axial direction. We scale lengths by d , times by the radial diffusion time $\frac{d^2}{\nu}$, azimuthal velocities by the velocity of the inner cylinder $\Omega_{cyl} r_1$, radial and axial velocities by $\frac{\nu}{d}$. Then

$$A = -\frac{\eta}{1+\eta}, \quad B = -\frac{A}{(1-\eta)^2} \quad (2.7a)$$

$$C = \frac{1+\eta}{1-\eta} \frac{1}{\ln \eta}, \quad D = C \ln(1-\eta) - \frac{1}{(1-\eta)^2} \quad (2.7b)$$

$$E = -\frac{1}{2} \left[1 + \frac{2\eta}{(1-\eta)^2} + C \right]. \quad (2.7c)$$

Here, $4Re/E = \partial_z p$ is the dimensionless axial pressure gradient driving the APF.

At the critical Taylor number $T_c(Re)$ [27,19,20,31], which depends on the through-flow rate, the basic flow becomes unstable to rotationally symmetric, axially extended PV perturbations via an oscillatory instability. There, a nonlinear PV solution branches off the basic flow in an axially infinite system. We consider the *deviation*

$$\mathbf{u}(r, z; t) = u\mathbf{e}_r + v\mathbf{e}_\varphi + w\mathbf{e}_z \quad (2.8)$$

of the velocity field from the basic flow (2.4) as the order-parameter field to characterize the secondary PV structure. We use the relative control parameter

$$\mu = \frac{T}{T_c(Re)} - 1 \quad (2.9a)$$

corresponding to

$$\epsilon = \frac{T}{T_c(Re=0)} - 1 \quad (2.9b)$$

to measure the distance from the onset of PV flow for $Re \neq 0$ and of stationary Taylor vortex flow for $Re = 0$, respectively. In this notation

$$\mu_c = 0 \quad \text{and} \quad \epsilon_c(Re) = \frac{T_c(Re)}{T_c(Re=0)} - 1 \quad (2.10)$$

is the critical threshold for onset of PV flow. The relation between μ and ϵ is

$$\mu = \frac{\epsilon}{1 + \epsilon_c(Re)}. \quad (2.11)$$

The shear forces associated with the axial through-flow slightly stabilize the homogeneous basic state, so $\epsilon_c(Re)$ slightly increases with Re [27,31–33]. For similar reasons a lateral Poiseuille shear flow suppresses the onset of convection rolls with axes perpendicular to the flow in a Bénard setup of a fluid layer heated from below [46,14].

A. Ginzburg-Landau description

Close to the bifurcation threshold $T_c(Re)$ of PV flow, i.e., for small μ , the flow has the form of a harmonic wave, e.g.,

$$w(r, z; t) = A(z, t) e^{i(k_c z - \omega_c t)} \hat{w}(r) + c.c. \quad (2.12)$$

with a complex amplitude $A(z, t)$ that is slowly varying in z and t . The critical wave number k_c , frequency ω_c [19,20,27,31–33], and eigenfunction $\hat{w}(r)$ [19,47] appearing in Eq. (2.12) have

been obtained from a linear stability analysis of the basic flow state as functions of Re . The complex vortex amplitude $A(z, t)$ is given by the solution of the 1D complex GLE

$$\begin{aligned} \tau_0 \left(\dot{A} + v_g A' \right) &= \mu (1 + ic_0) A + \xi_0^2 (1 + ic_1) A'' \\ &\quad - \gamma (1 + ic_2) |A|^2 A. \end{aligned} \quad (2.13)$$

Dot and primes denote temporal and spatial derivatives in the z -coordinate, respectively. All coefficients of the GLE have been calculated [27] as functions of Re for several radius ratios η . As a consequence of the system's invariance under the combined symmetry operation $\{z \rightarrow -z, Re \rightarrow -Re\}$ the coefficients τ_0, ξ_0^2, γ are even in Re while the group velocity v_g and the imaginary parts c_0, c_1, c_2 are odd in Re [15,27].

It should be noted that the control parameter range of μ over which (2.12) gives an accurate description of the full velocity field of PV flow, say, on a percent level is indeed very small: The asymmetry between radial in- and outflow intensities rapidly grows with μ and causes higher axial Fourier contributions $\sim e^{inkz}$ [48–50] to the velocity field that are discarded in the $\mu \rightarrow 0$ asymptotics of the GLE approximation (2.12). However, the modulus of the first Fourier mode of the vortex structures agrees for $Re = 0$ as well as for $Re \neq 0$ quite well with the one predicted by the GLE – cf. Sec. III. On the other hand, the PV structure selected according to the GLE differs from the one resulting from the full field equations – cf. Sec. IV.

B. Absolute and convective instability

For small ϵ and Re the control parameter plane is divided into three stability regimes – cf. Fig. 1 – characterized by different growth behavior of *linear* perturbations of the basic flow state. Below the critical threshold $\epsilon_c(Re)$ for onset of PV flow (dashed line in Fig. 1) any perturbation, spatially localized as well as extended, decays. This is the parameter regime of absolute stability of the basic state.

Perturbations of the basic state can grow only for $\epsilon > \epsilon_c(Re)$. However, in the presence of through-flow one has to distinguish [17] between the spatiotemporal growth behavior of

spatially localized perturbations and of spatially extended ones. The latter having a form $\sim e^{ikz}$ can grow above ϵ_c (Re) – in fact ϵ_c is determined as the stability boundary of the basic state against extended harmonic perturbations. On the other hand, a spatially localized perturbation, i.e., a wave packet of plane wave perturbations is advected in the so-called convectively unstable parameter regime faster downstream than it grows – while growing in the comoving frame it moves out of the system [17,18,36,51]. Thus, the downstream as well as the upstream facing intensity front of the vortex packet move into the same direction, namely, downstream. In this regime the flow pattern that results from a spatially localized source, which generates perturbations for a limited time only, is blown out of any system of finite length and the basic state is reestablished.

In the absolutely unstable regime (shaded region in Fig. 1) a localized perturbation grows not only in downstream direction but it grows and spatially expands also in upstream direction until the upstream propagating front encounters the inlet in a finite system. The final pattern resulting in such a situation shows in downstream direction a characteristic axial intensity profile under which the PV flow develops with increasing distance from the inlet.

Within the framework of the amplitude equation the boundary (full line in Fig. 1) between absolute and convective instability is given by [36]

$$\mu_{conv}^c = \frac{\tau_0^2 v_g^2}{4\xi_0^2 (1 + c_1^2)} \quad (2.14)$$

corresponding to $\epsilon_{conv}^c = \epsilon_c + (1 + \epsilon_c)\mu_{conv}^c$. Thus the absolutely unstable regime (shaded region in Fig. 1) is characterized by $\mu > \mu_{conv}^c$ or, equivalently, by the reduced group velocity

$$V_g = \frac{\tau_0}{\xi_0 \sqrt{(1 + c_1^2)} \mu} v_g = 2 \sqrt{\frac{\mu_{conv}^c}{\mu}} \quad (2.15)$$

being smaller than 2.

It should be mentioned that the GLE approximation (2.14) of μ_{conv}^c describes the boundary between absolute and convective instability resulting from the NSE [33,30] very well for the small Reynolds numbers considered here.

C. Methods of investigation

The linear growth analysis of modes $\exp[i(kz - \omega t + m\varphi)]$ shows that for small through-flow rates the homogeneous basic state becomes first unstable to axisymmetric PV flow [19,20,52]. Up to $Re = 4$ these patterns are also detected experimentally [25,28,29,31–33]. However, at larger Re one observes stationary spirals and mixed flow patterns [26,25] in addition to the bifurcation of propagating spirals [25,21–24,44]. The latter are predicted by the linear stability analysis to branch off the basic state at $Re \approx 20$ [19,20,52]. The PV patterns occurring at small through-flow rates ($Re < 4$) that are discussed here are rotationally symmetric. Therefore it is sufficient to solve the hydrodynamic field equations in an r - z cross section of the annulus to describe the resulting field $\mathbf{u}(r, z; t)$.

We have performed numerical simulations of the 2D NSE. They are compared with analytical and numerical results obtained from the 1D GLE. The latter was solved with a Crank-Nicholson algorithm using central differences for spatial derivatives with a resolution of 20 grid points per unit length d . The solution of the NSE was obtained with a time-dependent finite-differences marker and cell (MAC) algorithm [6,53] with pressure and velocity being iteratively adapted to each other with the method of artificial compressibility [54]. Also here the spatial resolution was 20 grid points per unit length d . The temporal stepsize was $1/1800$ times the radial diffusion time d^2/ν .

When comparing finite-differences solutions of the NSE with experiments or with analytical properties, e.g., of the GLE we take into account that the critical properties of the finite-differences MAC code differ slightly from the latter due to its finite spatiotemporal resolution. In particular the critical Taylor number, $T_c(Re)$, of the MAC code lies slightly (less than 1.5%) below the theoretical bifurcation threshold – cf. Table I and [27]. To find the marginal stability curve $T_{stab}(k)$ of the MAC algorithm for axially extended PV perturbations of wave number k we analyzed the complex growth rate $s(k)$ in systems of length $2\pi/k$ using periodic boundary conditions in axial direction for through-flow rates up to $Re = 5$. From this analysis we also obtained the critical values of the frequency ω_c , group

velocity v_g , wave number k_c , and the parameters τ_0 and ξ_0^2 (Table I). Furthermore, we have cross-checked these results by investigating the evolution of localized perturbations in long systems of lengths $\Gamma > 50$, in particular in the convectively unstable regime in a manner that is quite similar to experimental procedures [33,29]: We generated tiny, localized PV perturbations of about five vortex pairs with wave numbers close to k_c under an intensity envelope of Gaussian shape. They propagate downstream with the group velocity v_g . A fit to the rate of exponential growth of the envelope gives μ/τ_0 . From the growth of the full width at half maximum we obtain ξ_0^2/τ_0 . These identifications are based upon comparing with the temporal evolution of a Gaussian perturbation [36]

$$A(z, t = 0) \propto \exp\left[-\frac{z^2}{2\Delta_0^2}\right] \quad (2.16)$$

of initial axial extension Δ_0 according to the linearized GLE. It yields

$$A(z, t) \propto \frac{1}{\Delta(t)} \exp\left[\mu(1 + ic_0)\frac{t}{\tau_0} - \frac{(z - v_g t)^2}{2\Delta^2(t)}\right] \quad (2.17)$$

with

$$\Delta^2(t) = \Delta_0^2 + 2\xi_0^2(1 + ic_1)\frac{t}{\tau_0}. \quad (2.18)$$

Test runs with twice the lattice points per unit length showed that the differences between the critical properties of the continuous system that were obtained [27] with a shooting method and the finite-differences system significantly decrease by one order of magnitude.

We have also investigated the dependence of nonlinear, saturated PV flow on the numerical discretization. These tests show that the nonlinear vortex structures are basically independent of the discretization – provided it is not too coarse. However, one should base the comparison of bifurcated flow structures obtained with different discretizations on the relative control parameter $\mu = \frac{T}{T_c} - 1$ that is influenced via T_c by the discretization in question – see also Sec. IV B 3.

When comparing results obtained for different μ and Re from numerical simulations of the NSE with those following from the GLE we found it sometimes advantageous to present them as functions of the reduced group velocity V_g (2.15). The deviation

$$2 - V_g = 2 - 2\sqrt{\mu_{conv}^c/\mu} \quad (2.19)$$

is a scaled distance from the boundary between the absolutely and convectively unstable regime. Its relation to the through-flow Reynolds number Re and the Taylor number $T = (1 + \mu)T_c(Re)$ can be read off from Table I.

III. PROPAGATING VORTEX PATTERNS

We investigate PV patterns in the absolutely unstable regime in an annulus of finite length with two different end conditions: a basic state boundary condition (BCI) in Sec. III A and an Ekman vortex boundary condition (BCII) in Sec. III B. For both boundary conditions numerical simulations have been performed for the parameter combinations marked by symbols in Fig. 1. In each case we observe a pattern of vortices propagating downstream under a stationary intensity envelope after transients have died out as shown in Fig. 2. The oscillation frequency ω of the flow is independent of the radial and axial position while the local wave number k , the phase velocity $v_p = \omega/k$, and the vortex flow intensity varies with r and z . The frequency and the spatial variation of the PV pattern depends on the control parameters and on the boundary conditions but not on parameter history or initial conditions.

A. Basic state boundary condition – BCI

Here we discuss vortex suppressing boundary conditions that are realized by imposing the homogeneous basic state $\mathbf{U}(r)$ (2.4) at in- and outlet of the annulus. The flow resulting for this boundary condition resembles the experimental one of Babcock *et al.* [33]. There, a system of flow distributors and meshes at the inlet reduces external perturbations penetrating the interior of the annulus and seems also to suppress radial flow [55]. Near the inlet no *stationary* Ekman vortices are visible in this experiment and the amplitude of the downstream propagating vortices starts with zero or nearly zero [31–33].

To illustrate the global properties of the flow patterns we present in the upper part of Fig. 2 a hidden-line plot of the axial velocity field w . Thin lines show snapshots of w at the radial position $r = r_1 + 0.225$ obtained from the NSE at successive, equidistantly spaced times after transients have died out. Then vortices propagate downstream under a stationary intensity envelope (thick line). This envelope is determined by the temporal extrema of $w(r_1 + 0.225; t)$ at any z -position.

The oscillation frequency of the PV pattern is constant over the entire annulus. Sufficiently away from inlet and outlet we observe a bulk region of nonlinear saturated PV flow with spatially uniform amplitude and wavelength. With increasing through-flow this bulk pattern is pushed further and further downstream. The growth length l from the inlet over which the amplitude reaches half its saturation value depends on μ and Re . It increases and finally diverges when the control parameters μ , Re approach the absolute-convective instability border μ_c^{conv} , that is when V_g (2.15) reaches 2.

In Fig. 3 we compare the scaled growth length

$$L = \sqrt{\mu} l / \xi_0 \quad (3.1)$$

computed from the amplitude equation (solid line) with results from the NSE (symbols) for various combinations of ϵ and Re . Due to the scaling property of the GLE [14–16] keeping in mind the smallness of the imaginary parts c_i all values for l obtained by the GLE subject to BCI fall onto one curve in the plot of L vs. V_g . The open symbols representing the NSE results for BCI lie very close to the GLE curve. Full symbols for BCII are discussed in Sec. III B.

For further characterization of the PV flow structure we found a *temporal* Fourier decomposition of the time-periodic fields, e.g.,

$$w(r, z; t) = \sum_n w_n(r, z) e^{-in\omega t} \quad (3.2)$$

to be useful. To that end we first determined the oscillation frequency ω of the PV pattern and checked that it showed no spatial variation. In Fig. 4a the zeroth temporal Fourier mode

w_0 and the moduli $|w_1|$, $|w_2|$, and $|w_3|$ resulting from the NSE are shown by full lines while $|w_1|$ from the GLE is shown by the dashed one. The latter was rescaled by a factor of ≈ 0.94 which comes from comparing the first axial Fourier mode of $w(r = r_1 + 0.225)$ at $Re = 0$ in an axially periodic system with the GLE result of Recktenwald *et al.* [27,47]. As an aside we mention that for the radial velocity u having a nodeless radial profile with a single maximum the deviation of the first Fourier mode of $u(r = r_1 + 0.5)$ between finite-differences NSE and GLE is only 0.8% at $Re = 0$.

Note that the solution of the GLE (2.13)

$$A(z, t) = R(z)e^{i[\varphi(z) - \Omega t]} \quad (3.3)$$

oscillates harmonically with frequency Ω under a stationary envelope

$$R(z) = |A(z, t)| \quad (3.4)$$

after transients have died out. Therefore, the GLE velocity field (2.12) contains no temporal Fourier mode other than $n = 1$ whereas the solution of the full NSE has higher harmonics.

In the bulk region the *temporal* modes obtained for finite through-flow from the NSE grow for small μ proportional to $\mu^{n/2}$ with relative corrections proportional to μ . Thus, they show the same growth behavior with μ that the *axial* Fourier modes [48,57,58,49,50] of stationary Taylor vortices without through-flow show as a function of ϵ . The reason is that all fields in the PV state have the form of propagating waves

$$f_b(r, z; t) = f_b(r, z - \frac{\omega}{k_b}t) \quad (3.5)$$

in the bulk region - denoted by a subscript b. There the wave number k_b and the phase velocity ω/k_b do not vary with z .

The Fourier mode w_0 of the PV pattern is not zero everywhere since the variation of the flow amplitude under the fronts causes a secondary, stationary, closed flow pattern there - see, e.g., w_0 at $z \approx 9$ and near the outlet in Fig. 4a. Its strength and structure depends on the steepness of the front. For example, an increase of Re leads to a smaller gradient

of the upstream facing front and to weaker stationary secondary flow extending further downstream.

The intensity variation (cf. Figs. 2, 4a) of PV flow under the fronts also causes there a spatial variation in the local wavelength $\lambda(z)$ (Fig. 4b) and in the phase velocity $v_p(z) = \omega\lambda(z)/2\pi$ with the oscillation frequency ω of PV flow being constant. The full (dashed) line in Fig. 4b is the wavelength profile $\lambda(z)$ selected for BCI according to the NSE (GLE). This figure shows that the GLE does not describe the pattern selection quantitatively. The selected wavelength in the bulk region of the NSE (GLE) is smaller (larger) than the critical one – see also Sec. IV.

The local wavelength shown in Fig. 4b was determined from the phase gradient of the first temporal Fourier mode $w_1(z)$ at the radial position $r = r_1 + 0.225$. We have analyzed w_1 and also u_1 at other r positions and in addition we determined the axial distances between node positions of u and w . Under the fronts there is a significant radial variation of λ . Furthermore, the wavelengths determined via the phase gradients of w_1 and u_1 differ there from each other and from those obtained via node distances of w and u . But in the bulk part of the PV structure all these quantities yield the same wavelength λ_b .

B. Ekman vortex boundary condition – BCII

In Taylor-Couette experiments without through-flow rigid nonrotating end plates bounding the fluid in axial direction induce stationary Ekman vortex flow [2,4,59]. These vortices are also detected by Tsameret *et al.* in experiments with axial through-flow, where meshes at the apertures were used as nonrotating boundaries at in- and outlet [28,29].

The second axial boundary condition BCII enforces stationary Ekman vortices near the apertures of the annulus. To that end we impose at both ends $z = 0, \Gamma$ zero radial flow, zero azimuthal flow, and in axial direction the annular Poiseuille flow $W_{APF}(r)$ (2.6). The spatiotemporal properties of the vortex pattern subject to this BCII can be seen in the lower part of Fig. 2. There we show a hidden-line plot of the axial velocity in the same way and

for the same parameters as for the BCI pattern in the upper part of Fig. 2.

In the immediate vicinity of in- and outlet there are *stationary* Ekman vortices whose intensity rapidly decreases towards the bulk of the annulus. In addition there is – as in the BCI case – the PV flow structure that *oscillates* in time with a z-independent frequency ω . The oscillation amplitude drops to zero near the apertures due to the boundary conditions, and the stationary Ekman vortices increase the growth length l of the oscillating structure in comparison to the BCI case.

These two different flow elements are best separated by a temporal Fourier analysis. The results for BCII are shown in Fig. 5 for different through-flow rates. The zeroth temporal mode w_0 (thick line) represents the stationary Ekman vortex flow of the system. The temporally oscillating PV structure is characterized by the modes w_n (thin lines). The Ekman vortex structure at the inlet is only slightly affected by the through-flow: the strength of the Ekman vortex closest to the inlet decreases somewhat with increasing Re , while its extension slightly increases. The stationary vortices at the outlet become more and more squeezed together with increasing Re , and also their intensity reduces. On the other hand, the oscillatory pattern of PV responds dramatically to the through-flow in being more and more pushed downstream. Note also that for small Re where the PV amplitude of, say, $|w_1|$ overlaps near the inlet with the Ekman vortex intensity the latter causes axial oscillations in the harmonics of the PV flow and similarly near the outlet - cf. Fig. 5.

The filled symbols in Fig. 3 represent the growth length of the PV flow intensity. This length diverges in a similar way at the convective instability border $V_g = 2$ as the one obtained for BCI. But due to the presence of Ekman vortices at the inlet the characteristic growth length $l(\epsilon, Re)$ of PV flow is increased by $0.5 - 2.5d$ in comparison to the BCI case – Ekman vortices push the PV structure further downstream. The difference $l_{BCII} - l_{BCI}$ decreases with increasing through-flow rate as Ekman vortices and PV flow become more and more separated from each other.

As in the BCI case the zeroth temporal Fourier mode exhibits a secondary, stationary, closed flow pattern of low intensity under the fronts of the PV pattern. For small Reynolds

numbers this pattern is concealed by the Ekman vortex flow, whereas it becomes visible for bigger through-flow rates.

IV. PATTERN SELECTION

Our investigations of the PV structures show that the axial through-flow causes a unique pattern selection such that the selected structure is independent of history and initial conditions and depends only on the control parameters and boundary conditions. Thus, the axial flow causes possible wave numbers within the Eckhaus-stable band of stationary Taylor vortex patterns without through-flow to collapse to only one uniquely selected PV structure for nonvanishing through-flow rates. However, the PV patterns that are selected according to the GLE approximation and to the full NSE differ distinctly from each other. We first investigate in Sec. IV A the selection mechanism within the GLE framework. In Sec. IV B we compare with NSE results and experiments.

A. Pattern selection within the GLE

Here we elucidate how the pattern selection mechanism of the GLE can be understood as a nonlinear eigenvalue/boundary-value problem where the frequency of the PV pattern is the eigenvalue. Thus, the selected PV structure is characterized and determined by the combination of eigenvalue and corresponding eigenfunction.

1. The eigenvalue problem

We look for solutions of the GLE (2.13) of the form (3.3)

$$A(z, t) = a(z)e^{-i\Omega t} = R(z)e^{i[\varphi(z) - \Omega t]} \quad (4.1a)$$

with stationary envelope $R(z)$, stationary wave number

$$q(z) = k(z) - k_c = \varphi'(z), \quad (4.1b)$$

and constant frequency

$$\Omega = \omega - \omega_c. \quad (4.1c)$$

Inserting this solution ansatz into the GLE (2.13) one obtains the nonlinear eigenvalue problem

$$\begin{aligned} \tau_0 (-i\Omega a + v_g a') &= \mu (1 + ic_0) a + \xi_0^2 (1 + ic_1) a'' \\ &\quad - \gamma (1 + ic_2) |a|^2 a \end{aligned} \quad (4.1d)$$

or, equivalently,

$$\begin{aligned} i\tau_0(-\Omega + v_g q)R + \tau_0 v_g R' &= \mu(1 + ic_0)R \\ + \xi_0^2(1 + ic_1)(R'' - q^2 R + iq'R + 2iqR') &- \gamma(1 + ic_2)R^3 \end{aligned} \quad (4.1e)$$

as a solvability condition with Ω being the eigenvalue. We are interested in solutions $R(z)$ and $q(z)$ that look like the dashed lines in Fig. 4, i.e., where the variation of $R(z)$ and in particular of $q(z)$ is "as small as possible". Such a solution type seems to be connected with the eigenvalue Ω that is closest to zero. Here we consider the boundary conditions $R_{in,out} = 0$ at in- and outlet. These requirements fix four boundary conditions – namely, $Re(A_{in,out}) = Im(A_{in,out}) = 0$ – which are necessary to solve the GLE (2.13).

Note that the eigenfrequency Ω is in general determined by *global* properties and not by the *local* variation of the eigenfunctions $R(z)$ and $q(z)$, say, at the inlet or in the bulk. Nevertheless it is informative and useful for our further discussion to list below relations between Ω and structural properties at the inlet and in the bulk of the annulus.

2. Inlet behavior

From (4.1e) one finds that the BCI at in- and outlet, $R = 0$, implies the relation

$$R''_{in,out} = \left[\frac{\tau_0 v_g}{\xi_0^2 (1 + ic_1)} - 2iq_{in,out} \right] R'_{in,out} \quad (4.2)$$

at $z = 0, \Gamma$. Hence, whenever the modulus grows with finite slope, $R'_{in,out} \neq 0$, the boundary condition $R = 0$ fixes the wave number at inlet *and* outlet to the value $q_{in} = q_{out}$

$$\xi_0 q_{in,out} = -\frac{1}{2} c_1 \frac{\tau_0 v_g}{\xi_0 (1 + c_1^2)} = -\frac{c_1}{\sqrt{1 + c_1^2}} \sqrt{\mu_{conv}^c} \quad (4.3)$$

that depends only on Re . This value ensures that the imaginary part of the square bracket in (4.2) is zero. For $Re = 0$ one obtains $q_{in,out} = 0$ as Cross *et al.* [60]. In addition the condition $R = 0$ yields via the real part of (4.2) to two relations

$$R''_{in,out} = \frac{\tau_0 v_g}{\xi_0^2 (1 + c_1^2)} R'_{in,out} \quad (4.4)$$

between the different slopes $R'_{in} \neq R'_{out}$ and curvatures $R''_{in} \neq R''_{out}$ of the modulus at the two respective boundaries that hold independently of μ .

Furthermore, one can derive a relation between the eigenfrequency Ω , the wave number $q_{in,out}$, and its slope $q'_{in,out}$ at inlet and outlet. To that end we consider the axial derivative of (4.1e) at inlet and outlet with $R = 0$

$$\begin{aligned} & i\tau_0(\Omega - v_g q) + \mu(1 + ic_0) - \xi_0^2(1 + ic_1)q^2 \\ & -[\tau_0 v_g - 2iq\xi_0^2(1 + ic_1)]\frac{R''}{R'} = \xi_0^2(1 + ic_1)\left(\frac{R'''}{R''} + 3iq'\right). \end{aligned} \quad (4.5)$$

This allows to solve for $\frac{R'''}{R''}$ and q' separately. Using (4.3,4.4) one obtains the relation

$$\begin{aligned} \tau_0 \Omega &= (c_1 - c_0)\mu + \tau_0 v_g q_{in,out} \\ & - 3(1 + c_1^2)\xi_0^2 q'_{in,out}. \end{aligned} \quad (4.6)$$

Note that this equation implies $q'_{in} = q'_{out}$.

The relation (4.6) also demonstrates the nonlocality of the pattern selection mechanism and of the eigenvalue problem. At first sight one might be tempted to infer from the above relation between Ω and q_{in}, q'_{in} that the latter two fix the frequency. However, Eq. (4.6) equally well holds for q_{out}, q'_{out} and the outlet properties do not fix Ω neither. So the correct interpretation of Eq. (4.6) is that the eigenvalue Ω being the characteristic global signature of the pattern fixes the local quantities $q'_{in,out}$ for the given boundary conditions.

3. Bulk behavior

The wave number $q(z)$ away from in- and outlet in general differs from $q_{in}(=q_{out})$. In order to obtain the full axial profiles of the eigenfunctions $R(z)$ and $q(z)$ belonging to the eigenvalue Ω one has to solve the eigenvalue problem (4.1) with the boundary condition $R_{in,out} = 0$. Alternatively one can solve numerically the time-dependent GLE (2.13).

However, when the system size and the control parameters are such that the PV pattern forms a bulk part with a homogeneous modulus R_b and wave number q_b , i.e., where

$$R'_b = R''_b = q'_b = 0. \quad (4.7a)$$

Then, the dispersion relation

$$\tau_0 \Omega = (c_2 - c_0) \mu + \tau_0 v_g q_b + (c_1 - c_2) \xi_0^2 q_b^2 \quad (4.7b)$$

provides a relation between the frequency eigenvalue Ω , the bulk wave number q_b , and the bulk modulus

$$R_b^2 = \frac{\mu - \xi_0^2 q_b^2}{\gamma}. \quad (4.7c)$$

The equation (4.7b) establishes together with (4.6) also a relation between q_b on the one hand and $q_{in} = q_{out}$ and $q'_{in} = q'_{out}$ on the other hand.

4. Pattern selection at the convective instability boundary

Approaching the convective instability boundary (2.14) we found that q'_{in} decreases to zero so that the frequency eigenvalue becomes

$$\tau_0 \Omega_{conv}^c = -(c_0 + c_1) \mu_{conv}^c. \quad (4.8)$$

Then the bulk wave number approaches according to (4.8, 4.7b) the limiting value

$$\xi_0(q_b)_{conv}^c = -\frac{\sqrt{1 + c_1^{2(+)} - \sqrt{1 + c_2^2}}}{c_1 - c_2} \sqrt{\mu_{conv}^c}, \quad (4.9)$$

while the inlet wave number q_{in} is given by (4.3). Due to the very small imaginary parts c_i the solution (4.9) with the plus sign has to be discarded, since it corresponds to unphysically large wave numbers.

In Fig. 6 the bulk wavelengths selected according to the GLE are shown by halftone symbols. The results in the absolutely unstable regime, $V_g < 2$, were obtained numerically by integrating the time-dependent GLE (2.13). The value shown right at the border, $V_g = 2$, of the absolutely unstable regime is the analytical expression (4.9). Note that the selected GLE wavelengths are mostly larger than the critical one.

5. Comparison with front propagation

It is suggestive to compare properties of PV patterns like the one in the upper part of Fig. 2 with those behind an upstream facing front that connects in an axially infinite system the basic state at $z = -\infty$ with the developed PV state at $z = +\infty$. A *linear* growth analysis of the GLE (2.13) along the lines of [1, Sec. VI B 3] shows that the far tail of a *linear* front of PV perturbations moves with the front velocity

$$v_F = v_g - 2\frac{\xi_0}{\tau_0}\sqrt{\mu(1+c_1^2)}. \quad (4.10)$$

In the convectively unstable regime $0 < \mu < \mu_{conv}^c$ the front propagates downstream so that $v_F > 0$. In the absolutely unstable regime $\mu > \mu_{conv}^c$ it moves upstream, i.e., $v_F < 0$. And at the boundary $\mu = \mu_{conv}^c$ the front is stationary – $v_F = 0$. We compare the properties of such a stationary front at $\mu = \mu_{conv}^c$ with those of the solution $A(z, t)$ (3.3) with stationary modulus in a semi-infinite system ($0 \leq z < \infty$). The reason for restricting the comparison to μ_{conv}^c is that an upstream moving front in the absolutely unstable regime will be pushed against the inlet whence the spatiotemporal structure of the free front gets modified by the inlet.

The far tail of the stationary front resulting from the linear GLE is characterized by the local wave number

$$\xi_0 q_F(v_F = 0) = -\frac{c_1}{\sqrt{1+c_1^2}} \sqrt{\mu_{conv}^c} \quad (4.11)$$

and the oscillation frequency

$$\tau_0 \Omega_F(v_F = 0) = -(c_0 + c_1) \mu_{conv}^c. \quad (4.12)$$

In fact in the linear part of the stationary front the flow amplitude

$$A(z, t) \sim e^{i[Q_s z - \zeta(Q_s) t]} \quad (4.13)$$

varies with a wave number $Re(Q_s) = q_F$ (4.11), a spatial decay rate $Im(Q_s)$, a temporal growth rate $Im(\zeta(Q_s)) = 0$, and an oscillation frequency $Re(\zeta(Q_s)) = \Omega_F$ (4.12). Here

$$\xi_0 Q_s = -\frac{1}{2} \frac{i}{1+ic_1} \frac{\tau_0}{\xi_0} v_g = -\frac{i+c_1}{\sqrt{1+c_1^2}} \sqrt{\mu_{conv}^c} \quad (4.14)$$

is the saddle position of the complex dispersion relation

$$\tau_0 \zeta(Q, \mu) = \tau_0 v_g Q + i(1+ic_0)\mu - i(1+ic_1)\xi_0^2 Q^2 \quad (4.15)$$

of the linear GLE in the complex Q -plane determined by the condition

$$\left. \frac{d\zeta(Q)}{dQ} \right|_{Q_s} = 0 \quad (4.16)$$

for $v_F = 0$, i.e., at $\mu = \mu_{conv}^c$.

So the inlet wave number q_{in} (4.3) agrees with q_F (4.11) and Ω_{conv}^c (4.8) coincides with Ω_F (4.12). Thus, right at the border μ_{conv}^c of the absolutely unstable regime the frequency eigenvalue of the PV pattern growing in downstream direction from the inlet at $z = 0$ agrees with the oscillation frequency selected by the stationary, *linear* front. Within the front propagation point of view the PV pattern develops from the basic state with an exponential growth rate κ of the modulus. This leads for $R \rightarrow 0$ to $R' = \kappa R, R'' = \kappa^2 R, \dots \rightarrow 0$ for $z \rightarrow -\infty$. On the other hand, the PV flow intensity in the semi-infinite system in general drops to zero at the inlet with finite R' and R'' . Only at the border line $\mu = \mu_{conv}^c$ the difference disappears since there $R', R'', \dots \rightarrow 0$ for $z = 0$. In the absolutely unstable regime,

$V_g < 2$, the frequency eigenvalues $\Omega = \omega - \omega_c$ of the GLE lie slightly above the limiting value Ω_{conv}^c at the border of the absolutely unstable regime. The shaded symbols in Fig. 7 show for three different ϵ how Ω obtained numerically by integrating Eq. (2.13) approaches with increasing Re the front frequency $Re(\zeta(Q_s)) = \Omega_F(v_F = 0) = \Omega_{conv}^c$ (dashed line). For convenience, the merging points with this limit line are marked for the three ϵ -values investigated here by small halftone symbols.

Using this frequency for the full nonlinear PV pattern at μ_{conv}^c one obtains from the bulk dispersion relation (4.7b) an expression for the bulk wave number

$$\begin{aligned} \xi_0(q_b)_F &= \xi_0(q_b)_{conv}^c \\ &= -\frac{\sqrt{1+c_1^2}^{(+)}\sqrt{1+c_2^2}}{c_1-c_2}\sqrt{\mu_{conv}^c} \end{aligned} \quad (4.17)$$

far behind the front.

This bulk wave number behind the front has the opposite sign of the one that is cited in [28] and [29, Eqs. (10,14)]. An explanation for this might be that the formulas of Nozaki and Bekki [61, Eqs. 2, 8, and 9] that have been used in refs. [28,29] do not seem to have been transformed to a through-flow situation with an *upstream* facing front that joins in upstream direction to the basic state, in our case at $z = -\infty$. After correcting the sign error, the rough qualitative agreement that was reported in [28,29] between the experimental wave numbers [28,29] and the erroneous GLE results [28,29] disappears. In fact, both, the experiments [28,29] and our numerical simulations of the NSE yield wave numbers that differ in a common distinctive way from the proper GLE result (4.17).

As an aside we mention, that the *nonlinear* front solution of Nozaki and Bekki [61, Eqs. 2-7] yields for our GLE (2.13) a front that is not stationary at μ_{conv}^c but rather moves with velocity

$$v_{NB} = -\left(3\sqrt{\frac{1+c_1^2}{8+9c_1^2}} - 1\right)v_g \quad (4.18)$$

in upstream direction with a bulk wave number

$$\begin{aligned} \xi_0(q_b)_{NB} &= \frac{\sqrt{\mu_{conv}^c}}{(c_2 - c_1)\sqrt{8 + 9c_1^2}} \\ &\times \left[3(1 + c_1^2) + \text{sign}(c_2 - c_1)\sqrt{8(c_2 - c_1)^2 + 9(1 + c_1c_2)^2} \right]. \end{aligned} \quad (4.19)$$

So we conclude that the *nonlinear* front solution of Nozaki and Bekki is unrelated to the PV patterns at μ_{conv}^c . Furthermore, it was noted [62] that localized initial perturbations did not evolve into the *nonlinear* front solution of Nozaki and Bekki [61,63,64]. However, v_{NB} and $(q_b)_{NB}$ differ for small through-flow only slightly from the respective values $v_F = 0$ and $(q_b)_F$. For example at $Re = 2$ one obtains $v_{NB} = -0.06v_g$ and $(q_b)_{NB} = 1.15(q_b)_F$.

6. Scaling properties

Scaling length and times according to

$$\hat{z} = \sqrt{\mu} \frac{z}{\xi_0}; \quad \hat{t} = \mu \frac{t}{\tau_0}, \quad (4.20)$$

the GLE for the reduced amplitude $\hat{A} = A\sqrt{\gamma/\mu}$ does no longer contain γ and μ explicitly but the reduced group velocity V_g (2.15) and the coefficients c_0, c_1, c_2 . Thus the reduced selected frequency $\hat{\Omega} = \tau_0\Omega/\mu$ and the selected bulk wave number $\hat{q}_b = \xi_0q_b/\sqrt{\mu}$ depends not only on V_g but via c_0, c_1, c_2 also on the Reynolds number. This Re -dependence can alternatively be seen – via the Re -dependence of V_g and of the c_i 's entering (2.15) – also as an additional μ -dependence. The latter dependence is sufficiently strong to prevent a scaling of $\hat{\Omega}$ with V_g alone. However, by reducing the eigenfrequencies $\Omega(\epsilon, Re)$ selected for our three different ϵ -values by the limiting values $\Omega(\epsilon, Re_{conv}^c) = \Omega_{conv}^c$ (4.8) at the border of the absolutely unstable regime we effectively have eliminated the ϵ -dependence and all GLE data (halftone symbols in Fig. 8) fall onto one curve. A similar scaling holds for the bulk wave number q_b divided by $(q_b)_{conv}^c$ (4.9).

Remarkably enough, by reducing the NSE frequencies with the GLE frequency Ω_{conv}^c (4.8) the NSE results (open symbols in Fig. 8) almost show this one-variable scaling with

V_g . However, for the GLE $(\omega - \omega_c)/\Omega_{conv}^c$ increases monotonously with the scaled group velocity V_g whereas the NSE results show a monotonous decrease with V_g . This discrepancy between NSE and GLE results is caused by the different dispersion relations of the full hydrodynamic equations and the approximate GLE – cf. below.

B. Pattern selection within the NSE

Here we compare our numerical solutions of the NSE with results from the GLE and from experiments. First we discuss the selected wave numbers in the bulk region of PV flow. Then in comparison with front propagation we show common selection properties of NSE and GLE. Finally we compare with experiments.

1. Bulk wavelengths – NSE vs GLE

In Fig. 6 we show all selected bulk wavelengths obtained from numerical simulations of the NSE for BCI (open symbols) and BCII (filled symbols) in comparison with results obtained numerically from the GLE for BCI (halftone symbols). The NSE wavelengths that are selected when the basic state is enforced at in- and outlet weakly decrease with increasing Re and ϵ . For the smallest $\epsilon = 0.0288$ their values are very close to the critical wavelength λ_c (dotted line). For this boundary condition the wavelengths are mostly smaller than the critical one with a deviation of up to 2% for the largest $\epsilon = 0.186$ that was investigated here. These deviations are much stronger than the decrease of the critical wavelength with increasing Reynolds numbers.

It is interesting to note that transversal Rayleigh-Bénard convection rolls in horizontal shear flow [14,15] show a qualitative and quantitative [15, $\epsilon = 0.114$] correspondence to PV flow. Therefore, our results are not limited to PV flow in a Taylor-Couette apparatus only. In this context we also mention the experimental investigation of Gu and Fahidy [23]. They observed that axial through-flow causes a rearrangement of the vortex centers similar to the one seen for tranverse convection rolls subject to a horizontal flow [15, Fig. 2].

Without through-flow the vortices are aligned along a straight line roughly in the gap center. With increasing through-flow vortices are alternately displaced towards the outer or inner cylinder, thereby reducing the axial component of their distance and thus the wavelength. Viewed in the $z - r$ plane with r_2 above r_1 , right (left) turning vortices – for which w is negative (positive) close to the inner cylinder – are displaced towards the inner (outer) cylinder by a through-flow directed from left to right, since the through-flow enhances the axial flow component w of a right turning vortex near the outer cylinder at r_2 , and weakens it near the inner one at r_1 and vice versa for the left turning one.

Obviously the wavelengths resulting for BCI from the NSE (open symbols in Fig. 6) differ substantially and systematically from those resulting from the GLE (halftone symbols): the former decrease with growing Re and ϵ while the latter increase. Nevertheless we think – cf. the discussion in Sec. IV B 4 – that the selection mechanism is quite similar.

2. The effect of Ekman vortices

The NSE wavelengths obtained for the Ekman vortex generating BCII (filled symbols in Fig. 6) are similar to the BCI results in the limiting cases of small Re or small ϵ , and near the border line $V_g = 2$ of the absolutely unstable regime. In the vicinity of $V_g = 2$ the stationary Ekman vortices and the PV flow are spatially separated, and their interaction is very weak allowing for PV wavelengths like those for BCI. For very small Reynolds numbers the agreement in the PV wavelengths for BCI and BCII is not yet understood. In between there is a visible difference of up to 5% ($\epsilon = 0.186$ and $V_g \approx 0.4$) between the bulk wavelengths obtained for the two boundary conditions.

However, we found that the bulk phase velocities, $v_p = \omega/k$, were almost independent of the boundary conditions: the relative difference of v_p for BCI and BCII is less than 0.1% for the parameter regimes investigated here. Furthermore, the deviation of v_p from the critical value $(v_p)_c = \omega_c/k_c$ is less than about 1%. Hence, one can infer from the plots in Fig. 6 for $\lambda/\lambda_c - 1$ also the variation of the frequency eigenvalue with through-flow since

$$\frac{\omega}{\omega_c} - 1 = \frac{v_p}{(v_p)_c} \frac{k}{k_c} - 1 \simeq \frac{k}{k_c} - 1. \quad (4.21)$$

For the largest $\epsilon = 0.186$ we have observed for the Ekman vortex generating BCII an interesting behavior for very small $Re < 0.5$ ($V_g \lesssim 0.3$). For these parameters the PV pattern did not develop an axially homogeneous wavelength in the spatial region where the flow amplitude was indeed spatially uniform. Under these circumstances the wavelengths roughly show a linear variation with z between a larger value (upper small filled triangles in Fig. 6) at the upstream end of the bulk amplitude region and a smaller value (lower small filled triangles in Fig. 6) at the downstream end of the bulk region of constant flow amplitude. So the Ekman vortex at the inlet impedes the free downstream motion of the PV flow – it exerts a phase pinning force on the PV pattern that stretches the node distances. The situation is somewhat similar to the explicitly phase pinning boundary conditions that have been investigated in Rayleigh-Bénard convection with through-flow [65,15].

3. Finite size effects?

The selected wavelengths in the bulk region are practically independent of the system length as long as a saturation of the Taylor vortices takes place. To check this we performed a few simulations with aspect ratios $\Gamma = 25$ ($\epsilon = 0.114, Re = 2$, BCI and BCII) and $\Gamma = 10$ ($\epsilon = 0.114, 0.186, Re = 1$, BCI and BCII) and compared with the results obtained for our standard length $\Gamma = 50$. The change in the selected wavelength or frequency is less than 0.1% if the aspect ratio is halved to $\Gamma = 25$. In the system with length $\Gamma = 10$ no bulk region can be observed, therefore the wavelength can not reach a constant value. The oscillation frequency of the flow pattern is always independent of the axial position and mainly unchanged; the deviations are less than 0.5% even for the very short system of $\Gamma = 10$.

We have also investigated the dependence of nonlinear, saturated PV flow on the numerical discretization. These tests show that the nonlinear vortex structures are basically independent of the discretization – provided it is not too coarse – if one bases the comparison

of bifurcated flow structures obtained with different discretizations on the relative control parameter $\mu = \frac{T}{T_c} - 1$ that is influenced via T_c by the discretization in question [66].

4. Comparison with front propagation – NSE vs GLE

Let us first consider Taylor vortices without through-flow. Then the GLE (2.13) contains no imaginary coefficients c_i and the first-order spatial derivative is absent since $v_g = 0$. In this case the GLE yields for propagating fronts [67] as well as for stationary patterns in finite systems [60] the critical wave number, $q(z) = 0$, all over the extension of the pattern – the boundary condition $A = 0$ enforces the collapse of the supercritical band of stable bulk wave numbers of *nonlinear* vortex patterns to $q = 0$. This *nonlinearly* selected wave number $q = 0$ happens to be for $Re = 0$ the same as the wave number of maximal *linear* growth under a *linear* front whose spatiotemporal evolution is governed by the dispersion $\zeta_{GLE}(Q, \epsilon; Re = 0)$ (4.7b) of the *linear* GLE. In the presence of through-flow, however, the wave number of maximal growth under the *linear* front – e.g. q_F (4.11) – of the GLE differs from the one in the *nonlinear* bulk far behind the front [$(q_b)_F$ (4.17)].

Now, already without through-flow the dispersion relation of the *linear* NSE differs significantly from that of the GLE so that the wave number of largest temporal growth under a *linear* NSE front deviates from the GLE result $q = 0$. As an aside we mention that a somewhat similar behavior has also been observed experimentally [3,10] and numerically for Taylor vortices [6,68] or Rayleigh-Bénard convection rolls [11] which, however, were located in the nonlinear part of propagating fronts. In this context it is useful to keep in mind that the wavelength profile $\lambda(z)$ of numerically obtained Taylor vortex fronts [6,68] shows an axial variation with a characteristic dip in the steepest region of the front similar to the one of the full line in Fig. 4b near $z = 8$.

Now let us consider the through-flow case. In Fig. 7 we compare the eigenfrequencies of the *nonlinear* NSE (open symbols) for BCI with those (solid line) that would be selected by a *linear* front that is stationary at the border of the absolutely unstable regime. To that

end Recktenwald and Dressler [30] have determined the dispersion relation $\zeta(Q)$ of linear perturbations $\sim e^{i[(k_c+Q)z-(\omega_c+\zeta)t]}$ in the complex Q -plane resulting from the NSE with a shooting method as described in ref. [33]. The solid line in Fig. 7 represents the frequency $\Omega_F = Re(\zeta(Q_s))$ selected by the stationary front ($v_F = 0$) of the *linear* NSE. Again, as discussed for the GLE in Sec. IV A 5, this frequency is determined by the saddle Q_s of $\zeta(Q)$ for which the temporal growth rate $Im \zeta(Q_s) = 0$. This defines the boundary between absolute and convective instability. With increasing Re the eigenfrequency of the *nonlinear* NSE approaches the frequency selected by the *linear* stationary front at the border of the absolutely unstable regime as indicated for the three ϵ -values shown in Fig. 7. The front frequencies for these ϵ -values are marked by small open symbols on the curve $Re(\zeta(Q_s))$ to indicate that the eigenfrequencies of the NSE in the absolutely unstable regime (large open symbols in Fig. 7) do indeed end at the right positions on this curve.

This NSE behavior is very similar to the GLE behavior (halftone symbols and dashed line). Note, however, that the linear dispersion relations of NSE and GLE are different: the front frequency $Re(\zeta_{NSE}(Q_s)) \simeq 0.0072Re + 0.0056Re^3$ (solid line in Fig. 7) is positive and increases with through-flow while $Re(\zeta_{GLE}(Q_s)) \simeq -0.0002Re - 0.0062Re^3$ (dashed line) is negative and decreases with through-flow. This difference in the dispersion relations seems to be the major cause for the differences in the selected patterns.

5. Comparison with experiments

In early experiments by Snyder [21,22] or Takeuchi and Jankowski [20] the distinction between absolute and convective instability was not yet established. PV patterns were observed with wavelengths below the critical one for Reynolds numbers $Re < 10$ [21,22]. However, a pattern selection was not reported. The wavelengths were seen to vary up to 7% from run to run for the same control parameter combinations and in some cases 5% over the spatial extension. Furthermore, the vortex spacings did not change after the occurrence of PV flow when increasing the relative Taylor number up to $\epsilon = 0.15$ [22].

Takeuchi and Jankowski [20] obtained wavelengths below the critical one for example with a deviation of $\approx -2.5\%$ for $Re = 9.4, \epsilon \approx 0.06, \eta = 0.5$ that is in the same order of magnitude of our NSE results in the absolute instability regime.

The experimental results of Tsameret and Steinberg [28,29] exhibit a unique selection, similar to the results presented here. Their wavelengths [28] are always less than the critical one for axial boundaries that enforce stationary Ekman vortex flow. However, in contrast to our results they observed no ϵ dependence of the selected wavelengths but an Re dependence that is much stronger than ours leading to a relative deviation from λ_c of up to -10% at $Re \approx 3$ for $\eta = 0.707$ [28]. In addition their phase velocity of PV flow, $v_p = 1.055Re$ [28], is much smaller than ours, which is close to the critical one. All wavelengths observed for through-flow rates above $Re = 1$ belong to noise sustained structures in the convectively unstable region [29], which leads to deviations from λ_c of about 3% when one limits the comparison to the regime of absolute instability. Since the ϵ -values at which the measurements of [28,29] were performed are not given we have estimated an ϵ -value of ≈ 0.025 based on the convective instability border at $Re = 1$. For this ϵ the above mentioned 3% deviation of λ from λ_c is an order of magnitude larger than our NSE results or the results (4.9) of the GLE.

On the other hand, the experimental wave number found in [25] for a known, published $\epsilon \approx 0.38$ and Re up to 4 can be compared directly with our results to check the predicted ϵ and Re dependence. In this case all experimental wavelengths [25] decrease up to 10% below the critical one at $Re \approx 3.7$ whereas we would expect from our simulations and from [14,15] less than half the deviation from λ_c .

V. CONCLUSION

We have investigated propagating vortex structures in an axial flow for different realistic axial boundary conditions in systems of finite length. Within the subregion of absolute instability a unique pattern selection is observed. The selected PV flow structures are independent of parameter history, initial conditions, and system's length (provide it is large

enough to allow for a nonlinear, saturated, homogeneous bulk region). But they depend on the axial boundary conditions. For conditions enforcing the basic state at the boundaries as well as for conditions that enforce stationary Ekman vortex flow near the boundaries the PV pattern is suppressed at the inlet and outlet of the annulus. Then one observes a characteristic stationary axial intensity and wave number profile, whereas the oscillation frequency of the pattern is constant all over the system. The analysis of the appropriate Ginzburg-Landau equation for PV flow shows that the selected frequency of the pattern oscillation is the eigenvalue of a nonlinear eigenvalue problem for which the axial variation of the corresponding eigenfunction is smooth and as small as possible. The eigenfunction is the complex pattern amplitude that characterizes the intensity and wave number profiles of the PV structure. The GLE intensity profiles agree well with those of the NSE. However, there are characteristic differences in the selected frequencies and wave number profiles of the full NSE and the GLE approximation. They are identified to be mainly caused by the different dispersion relations of the equations. Approaching the border between absolute and convective instability the eigenvalue problem becomes effectively linear and the pattern selection mechanism becomes that one of linear front propagation.

ACKNOWLEDGMENTS

This work was supported by the Deutsche Forschungsgemeinschaft and the Stiftung Volkswagenwerk.

REFERENCES

- [1] M. C. Cross and P. C. Hohenberg, *Rev. Mod. Phys.* **65**, 851 (1993).
- [2] G. Ahlers, D. S. Cannell, M. A. Dominguez-Lerma, and R. Heinrichs, *Physica D* **23**, 202 (1986).
- [3] G. Ahlers and D. S. Cannell, *Phys. Rev. Lett.* **50**, 1583 (1983).
- [4] R. Heinrichs, G. Ahlers, and D. S. Cannell, *Phys. Rev. Lett.* **56**, 1794 (1986).
- [5] M. Lücke, M. Mihelcic, B. Kowalski, and K. Wingerath, in *The Physics of Structure Formation*, edited by W. Güttinger and G. Dangelmayr (Springer-Verlag, Berlin, 1987), p. 97.
- [6] M. Lücke, M. Mihelcic, and K. Wingerath, *Phys. Rev. A* **31**, 396 (1985).
- [7] H. Riecke and H. G. Paap, *Phys. Rev. A* **33**, 547 (1986); *Phys. Rev. Lett.* **59**, 2570 (1987).
- [8] V. Croquette, *Contemp. Phys.* **30**, 113, 153 (1989)
- [9] I. Rehberg, E. Bodenschatz, B. Winkler, and F. H. Busse, *Phys. Rev. Lett.* **59**, 282 (1987).
- [10] J. Fineberg and V. Steinberg, *Phys. Rev. Lett.* **58**, 1332 (1987).
- [11] M. Lücke, M. Mihelcic, and B. Kowalski, *Phys. Rev. A* **35**, 4001 (1987).
- [12] P. Kolodner, *Phys. Rev. A* **46**, 6431 (1992).
- [13] G. W. Baxter, K. D. Eaton, and C. M. Surko, *Phys. Rev. A* **46**, 1735 (1992).
- [14] H. W. Müller, M. Lücke, and M. Kamps, *Europhys. Lett.* **10**, 451 (1989).
- [15] H. W. Müller, M. Lücke, and M. Kamps, *Phys. Rev. A* **45**, 3714 (1992).
- [16] H. W. Müller, M. Lücke, and M. Kamps, in *Ordered and Turbulent Patterns in Taylor*

- Couette Flow*, edited by D. Andereck and F. Hayot, Vol. 297 of NATO ASI Series B (Plenum, New York, 1992), p. 187.
- [17] A. Bers, in *Basic Plasma Physics I*, edited by A. A. Galeev and R. N. Sudan (North-Holland, New York, 1983); R. J. Briggs, *Electron Stream Interaction with Plasmas* (MIT Press, Cambridge, MA, 1964).
- [18] P. Huerre and P. A. Monkewitz, *Ann. Rev. Fluid Mech.* **22**, 473 (1990); *J. Fluid Mech.* **159**, 151 (1985), P. Huerre, in *Instabilities and Nonequilibrium Structures*, edited by E. Tirapegui and D. Villarroel (Reidel, Dordrecht, 1987), p. 141.
- [19] K. C. Chung and K. N. Astill, *J. Fluid Mech.* **81**, 641 (1977).
- [20] D. J. Takeuchi and D. F. Jankowski, *J. Fluid Mech.* **102**, 101 (1981).
- [21] H. A. Snyder, *Proc. R. Soc. London Ser. A* **265**, 198 (1961).
- [22] H. A. Snyder, *Ann. Phys.* **31**, 292 (1965).
- [23] Z. H. Gu and T. Z. Fahidy, *Can. J. Chem. Eng.* **63**, 710 (1985); *ibid.* **63**, 14 (1985).
- [24] Z. H. Gu and T. Z. Fahidy, *Can. J. Chem. Eng.* **64**, 185 (1986).
- [25] A. Tsameret and V. Steinberg, *Phys. Rev. E* **49**, 4077 (1994).
- [26] R. M. Lueptow, A. Docter, and K. Min, *Phys. Fluids A* **4**, 2446 (1992).
- [27] A. Recktenwald, M. Lücke, and H. W. Müller, *Phys. Rev. E* **48**, 4444 (1993).
- [28] A. Tsameret and V. Steinberg, *Europhys. Lett.* **14**, 331 (1991).
- [29] A. Tsameret and V. Steinberg, *Phys. Rev. E* **49**, 1291 (1994).
- [30] A. Recktenwald and M. Dressler (private communication).
- [31] K. L. Babcock, G. Ahlers, and D. S. Cannell, *Phys. Rev. Lett.* **24**, 3388 (1991).
- [32] K. L. Babcock, D. S. Cannell, and G. Ahlers, *Physica D* **61**, 40 (1992).

- [33] K. L. Babcock, G. Ahlers, and D. S. Cannell, *Phys. Rev. E* **50**, 3670 (1994).
- [34] A. Tsameret and V. Steinberg, *Phys. Rev. Lett.* **67**, 3392 (1991).
- [35] A. Tsameret, G. Goldner, and V. Steinberg, *Phys. Rev. E* **49**, 1309 (1994).
- [36] R. J. Deissler, *J. Stat. Phys.* **40**, 371 (1985); *ibid.* **54**, 1459 (1989); *Physica D* **25**, 233 (1987); *ibid.* **18**, 467 (1986).
- [37] For review of the Taylor-Couette system without axial through-flow see R. C. DiPrima and H. L. Swinney, in *Hydrodynamic Instabilities and Transition to Turbulence*, edited by H. L. Swinney and J. P. Gollub (Springer, Berlin, 1981), p. 139.
- [38] S. Goldstein, *Proc. Cambridge Philos. Soc.* **33**, 41 (1937).
- [39] R. J. Cornish, *Proc. R. Soc. London Ser. A* **140**, 227 (1933); A. Fage, *Proc. R. Soc. London Ser. A* **165**, 501 (1938).
- [40] S. Chandrasekhar, *Proc. Nat. Acad. Sci. USA* **46**, 141 (1960); *Proc. R. Soc. London Ser. A* **265**, 188 (1962); R. C. DiPrima, *J. Fluid Mech.* **9**, 621 (1960); S. Datta, *J. Fluid Mech.* **21**, 635 (1965); E. R. Krueger and R. C. DiPrima, *J. Fluid Mech.* **19**, 528 (1964); T. H. Hughes and W. H. Reid, *Philos. Trans. R. Soc. London Ser. A* **263**, 57 (1968); L. Elliott, *Phys. Fluids* **16**, 577 (1973);
- [41] M. A. Hasoon and B. W. Martin, *Proc. R. Soc. London Ser. A* **352**, 351 (1977).
- [42] R. C. DiPrima and A. Pridor, *Proc. R. Soc. London Ser. A* **366**, 555 (1979).
- [43] K. Bühler and F. Polifke, in *Nonlinear Evolution of Spatio-temporal Structures in Dissipative Continuous Systems*, edited by F. Busse and L. Kramer (Plenum Press, New York, 1990), p. 21; K. W. Schwarz, B. E. Springett, and R. J. Donnelly, *J. Fluid Mech.* **20**, 281 (1964); R. J. Donnelly and D. Fultz, *Proc. Nat. Acad. Sci. USA* **46**, 1150 (1960); N. Gravas and B. W. Martin, *J. Fluid Mech.* **86**, 385 (1978); P. L. Greaves, R. I. Grosvenor, and B. W. Martin, *Int. J. Heat & Fluid Flow* **4**, 187 (1983); D. A. Sim-

- mers and J. E. R. Coney, *J. Mech. Engng. Sci.* **21**, 59 (1979); M. M. Sorour and J. E. R. Coney, *J. Mech. Engng. Sci.* **21**, 397 (1979).
- [44] K. Kataoka, H. Doi, T. Hongo, and M. Futagawa, *Chem. Eng. of Japan* **8**, 472 (1975);
- [45] S. Chandrasekhar, *Hydrodynamic and Hydromagnetic Stability* (Dover Publications, New York, 1961).
- [46] For a review see, e. g., R. E. Kelly, *Adv. Appl. Mech.* **31**, 35 (1994).
- [47] A. Recktenwald, *Diplom thesis*, Universität des Saarlandes, 1991 (unpublished).
- [48] R. Heinrichs, D. S. Cannell, G. Ahlers, and M. Jefferson, *Phys. Fluids*. **31**, 250 (1988).
- [49] M. Lücke and D. Roth, *Z. Phys. B* **78**, 147 (1990).
- [50] D. Roth, M. Lücke, M. Kamps, and R. Schmitz, in *Ordered and Turbulent Patterns in Taylor Couette Flow*, edited by D. Andereck and F. Hayot, Vol. 297 of NATO ASI Series B (Plenum, New York, 1992), p. 59.
- [51] R. Tagg, W. S. Edwards, and H. Swinney, *Phys. Rev. A* **42**, 831 (1990).
- [52] B. S. Ng and E. R. Turner, *Proc. R. Soc. London Ser. A* **382**, 83 (1982).
- [53] J. E. Welch, F. H. Harlow, J. P. Shannon, and B. J. Daly, Los Alamos Scientific Laboratory Report of the University of California, Report No. LA-3425, 1966 (unpublished); G. P. Williams, *J. Fluid Mech.* **37**, 727 (1969); F. H. Harlow and J. E. Welch, *Phys. Fluids* **8**, 2183 (1965).
- [54] C. W. Hirt, B. D. Nichols, and N. C. Romero, Los Alamos Scientific Laboratory Report of the University of California, Report No. LA-5852, 1975 (unpublished); J. A. Vieceili, *J. Comput. Phys.* **8**, 119 (1971); A. J. Chorin, *Math. Comp.* **22**, 745 (1968).
- [55] There is an entrance chamber designed such that the fluid enters the annulus with no azimuthal velocity and with a plug flow like profile of the axial velocity [33]. Thus, an

Ekman vortex is not induced near the inlet. The annular Poiseuille flow develops faster than the circular Couette flow [56]. The development length towards the homogeneous base flow measured by Babcock *et al.* [33] is about $1.5d$ for $Re = 3$.

- [56] K. N. Astill, J. T. Ganley, and B. W. Martin, Proc. R. Soc. London Ser. A **307**, 55 (1968); J. E. R. Coney and D. A. Simmers, J. Mech. Engng. Sci. **21**, 19 (1979); B. W. Martin and M. A. Hasoon, J. Mech. Engng. Sci. **18**, 221 (1976); B. W. Martin and A. Payne, Proc. R. Soc. London Ser. A **328**, 123 (1972).
- [57] A. Davey, J. Fluid Mech. **14**, 336 (1962).
- [58] H. Kuhlmann, D. Roth, and M. Lücke, Phys. Rev. A **39**, 745 (1989).
- [59] G. Pfister and I. Rehberg, Phys. Lett. A **83**, 19 (1981).
- [60] M. C. Cross, P. G. Daniels, P. C. Hohenberg, and E. D. Siggia, J. Fluid Mech. **127**, 155 (1983).
- [61] K. Nozaki and N. Bekki, Phys. Rev. Lett. **51**, 2171 (1983).
- [62] W. van Saarloos and P. C. Hohenberg, Physica D **56**, 303 (1992).
- [63] K. Nozaki and N. Bekki, J. Phys. Soc. Jpn **53**, 1581 (1984).
- [64] R. Conte and M. Musette, Physica D **69**, 1 (1993).
- [65] A. Pocheau, V. Croquette, P. Le Gal, and C. Poitou, Europhys. Lett. **3**, 915 (1987).
- [66] Using discretizations of $n = 15, 20$, and 30 lattice points per unit length we observe a systematic deviation in the selected wave numbers of the nonlinear PV patterns. For $T = 2870$, $Re = 0.75$ and the boundary condition BCII (Sec. III B) the selected wavelength of the saturated PV flow is $\lambda = 2.102, 2.089, 2.076$ for $n = 15, 20, 30$, respectively. A coarser grid provides a smaller $T_c(Re)$ and a bigger λ which is in agreement with Fig. 6. In the case of BCI (Sec. III A) the coarser grid decreases the wavelength $\lambda = 1.949, 1.952, 1.953$ for $n = 15, 20, 30$ at $T = 2870$ and $Re = 3.1$ also in agreement with Fig. 6. By using

the relative control parameter μ (2.9a) with the appropriate $T_c(Re)$ these systematic deviations practically disappear.

[67] G. Dee and J. S. Langer, Phys. Rev. Lett. **50**, 383 (1983).

[68] M. Niklas, *Ph. D. thesis*, RWTH Aachen, 1988 (unpublished).

TABLES

TABLE I. Bold-faced numbers denote critical values and coefficients that are appropriate for the finite-differences code with spatial grid size 0.05 used in our simulations of the NSE and that have been used for scaling the NSE results. The methods for determining these numbers are described in Sec. II C. The imaginary parts c_1 , c_2 , c_3 are taken from ref. [27]. γ depends on the normalization of the linear radial eigenfunction $\hat{u}(r)$ which was chosen to be $|\hat{u}(r_1 + 0.5)| = 15.2$.

$a = a_0 \left[1 + \frac{a_2}{ a_2 } (Re/a_2)^2 \right]$					
	T_c	k_c	ξ_0^2	τ_0	γ
a_0	2420.23	3.1305	0.144	0.0762	8.06
a_2	138.62	252.96	-27.23	-49.68	-12.33
$a = a_1 Re \left[1 + \frac{a_3}{ a_3 } (Re/a_3)^2 \right]$					
	v_g	ω_c	c_0	c_1	c_2
a_1	1.20	3.647	1/138	1/40.7	1/287
a_3	–	–	-51.8	70.5	-97.8

FIGURES

FIG. 1. Stability domains of the basic flow state (2.4) in the plane of control parameters. Numerical simulations have been performed for the parameters marked by circles ($\epsilon = 0.0288$), diamonds ($\epsilon = 0.114$), and triangles ($\epsilon = 0.186$). Dashed line is the critical threshold for onset of extended PV flow and full line the boundary (2.14) between absolute and convective instability. The parameters entering (2.14) – cf. Table I – characterize the finite-differences version of the NSE. They have been obtained with the methods described in Sec. II C.

FIG. 2. Spatiotemporal structure of PV flow. Thin lines show vertically displaced snapshots of the axial velocity field $w(r_1 + 0.225, z; t)$ at successive, equidistantly spaced times. Thick lines show the stationary envelopes. The BCI at inlet and outlet suppresses any vortex flow there, while the BCII suppresses PV flow but induces *stationary* Ekman vortices. Parameters are $\epsilon = 0.114$ and $Re = 2.5$.

FIG. 3. Scaled growth length L (3.1) of PV structures vs scaled group velocity V_g (2.15). Symbols represent lengths obtained from the NSE for different combinations (cf. Fig. 1) of Re and $\epsilon = 0.0288$ (circles), $\epsilon = 0.114$ (diamonds), and $\epsilon = 0.186$ (triangles). Boundary conditions are BCI for open symbols and BCII for filled ones. The line shows the scaling behavior of the GLE subject to BCI.

FIG. 4. Structure of PV flow selected for BCI at inlet and outlet. Shown are the axial variations of the *temporal* Fourier modes (a) and of the wavelength (b) of $w(r_1 + 0.225, z; t)$. Full lines result from numerical simulations of the full NSE. Dashed lines come from the GLE. Parameters are $\epsilon = 0.114$ and $Re = 2.5$.

FIG. 5. Axial structure of vortex patterns subject to BCII. The zeroth temporal Fourier mode w_0 (thick lines) of the axial velocity field $w(r_1 + 0.225, z; t)$ reflects the stationary Ekman vortices. The modes w_n with $n > 0$ (thin lines) characterize the oscillating PV pattern. Parameters are $\epsilon = 0.114$ and $Re = 1.0$ (a), 2.5 (b), 2.7 (c).

FIG. 6. Selected wavelengths in the bulk region of PV structures vs scaled group velocity V_g (2.15). Open (halftone) symbols refer to the NSE (GLE) subject to BCI at inlet and outlet. Filled symbols refer to the NSE subject to BCII at inlet and outlet. Parameters are $\epsilon = 0.0288$ (circles), $\epsilon = 0.114$ (diamonds), and $\epsilon = 0.186$ (triangles). The small filled triangles are explained in Sec. IV B2.

FIG. 7. Selected oscillation frequency of PV flow obtained with BCI from the NSE (open symbols) and GLE (halftone symbols) vs Reynolds number. The full (dashed) line is the front frequency $\Omega_F = \text{Re}(\zeta(Q_s))$ of the linearized NSE (GLE) at the border between absolute and convective instability. Parameters are $\epsilon = 0.0288$ (circles), $\epsilon = 0.114$ (diamonds), and $\epsilon = 0.186$ (triangles). The small symbols marking Ω_F for these three ϵ values show that the eigenfrequencies of the nonlinear equations in the absolutely unstable regime approach the Ω_F limit curve at the right places.

FIG. 8. Frequency shift $\omega - \omega_c$ of PV flow vs scaled group velocity V_g (2.15) for BCI. Both, NSE (open symbols) and GLE (halftone symbols) results are scaled by the corresponding GLE frequency Ω_{conv}^c (4.8) at the convective instability border for the respective parameters $\epsilon = 0.0288$ (circles), $\epsilon = 0.114$ (diamonds), and $\epsilon = 0.186$ (triangles). The small symbols have the same meaning as explained in Fig. 7.

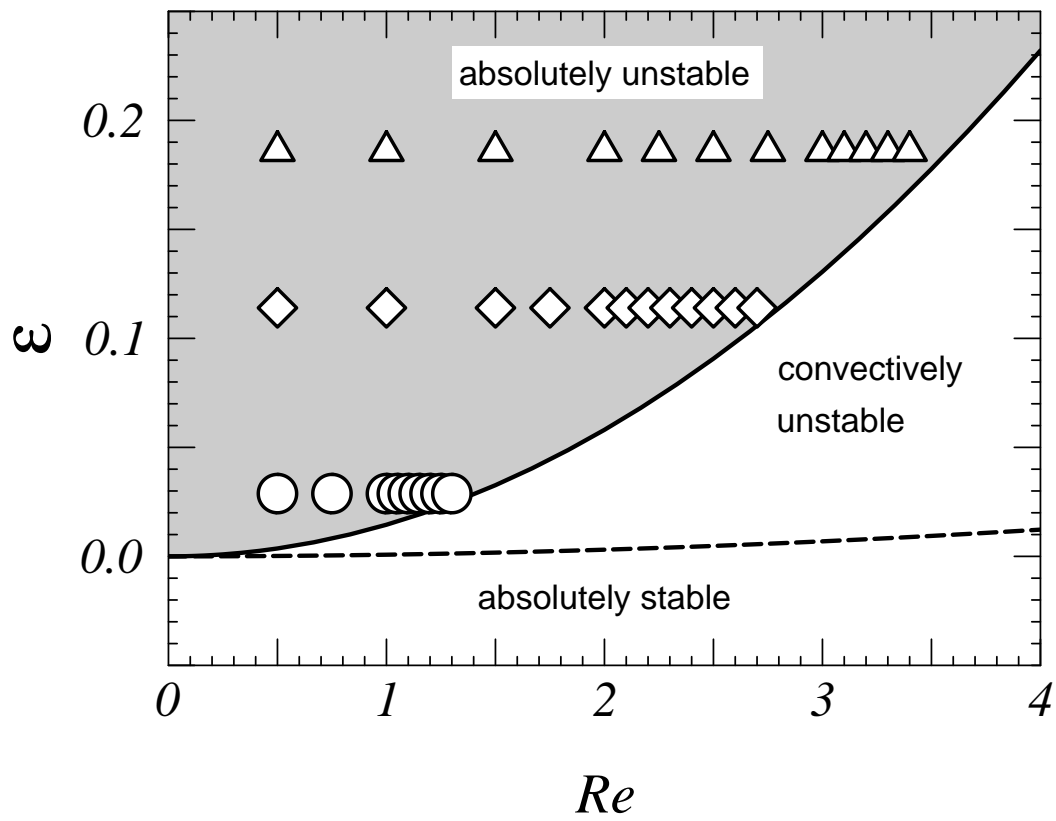


Figure 1
 Pattern selection in the absolutely unstable regime

P. Büchel et al., Phys. Rev. E

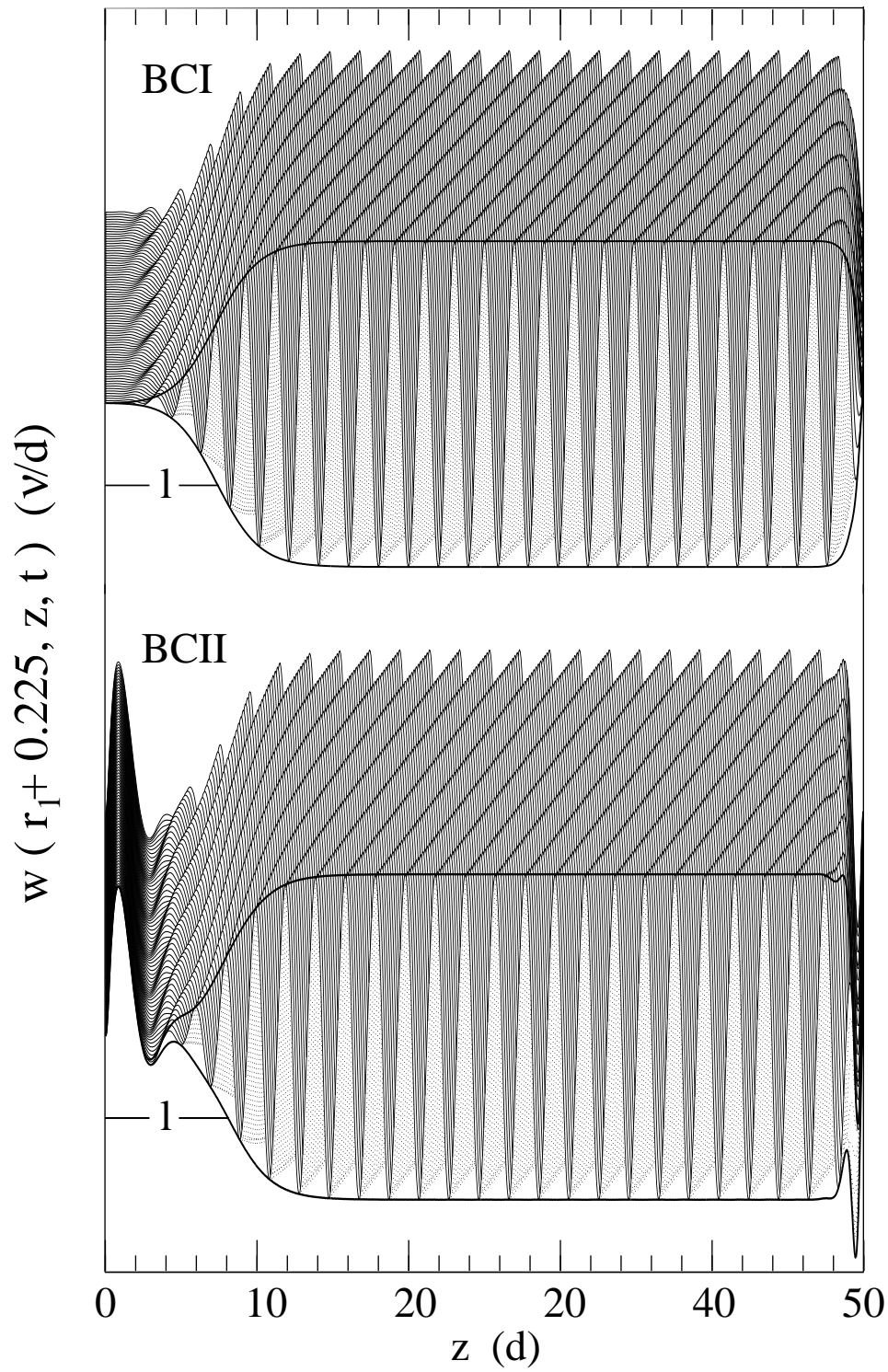


Figure 2
 Pattern selection in the absolutely unstable regime

P. Büchel et al., Phys. Rev. E

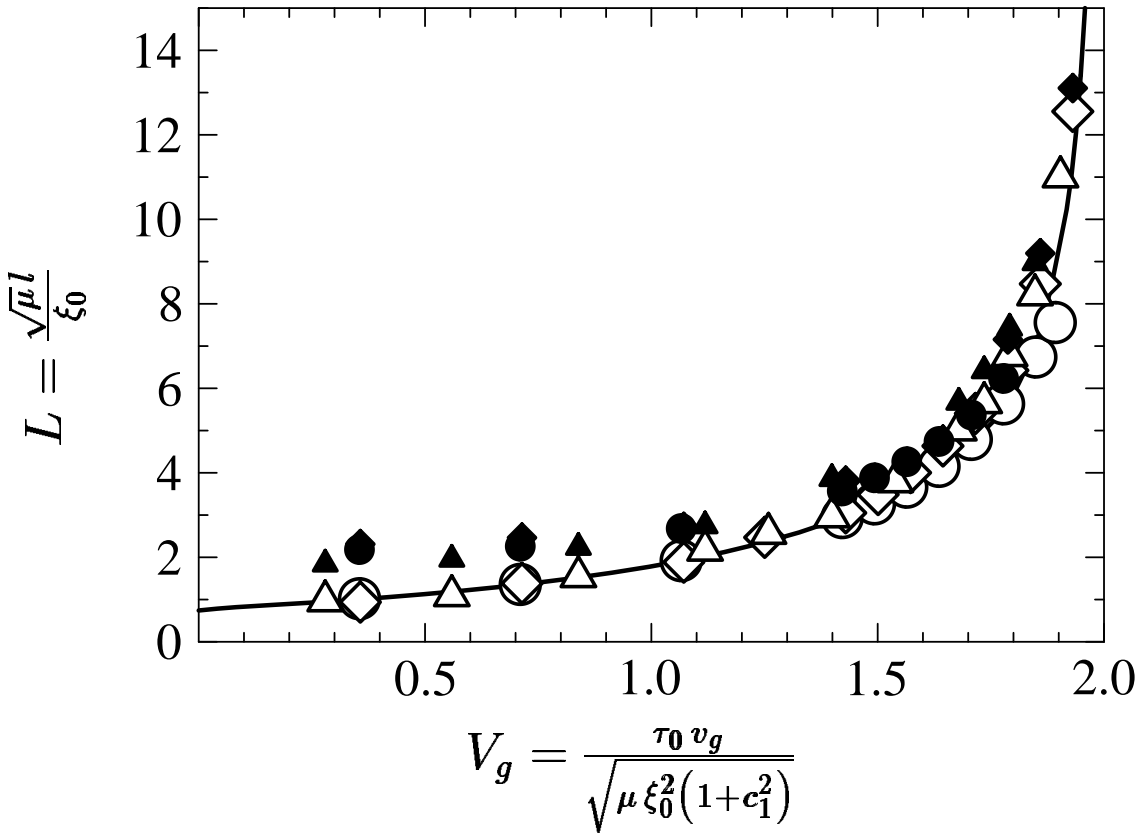


Figure 3
 Pattern selection in the absolutely unstable regime

P. Büchel et al., Phys. Rev. E

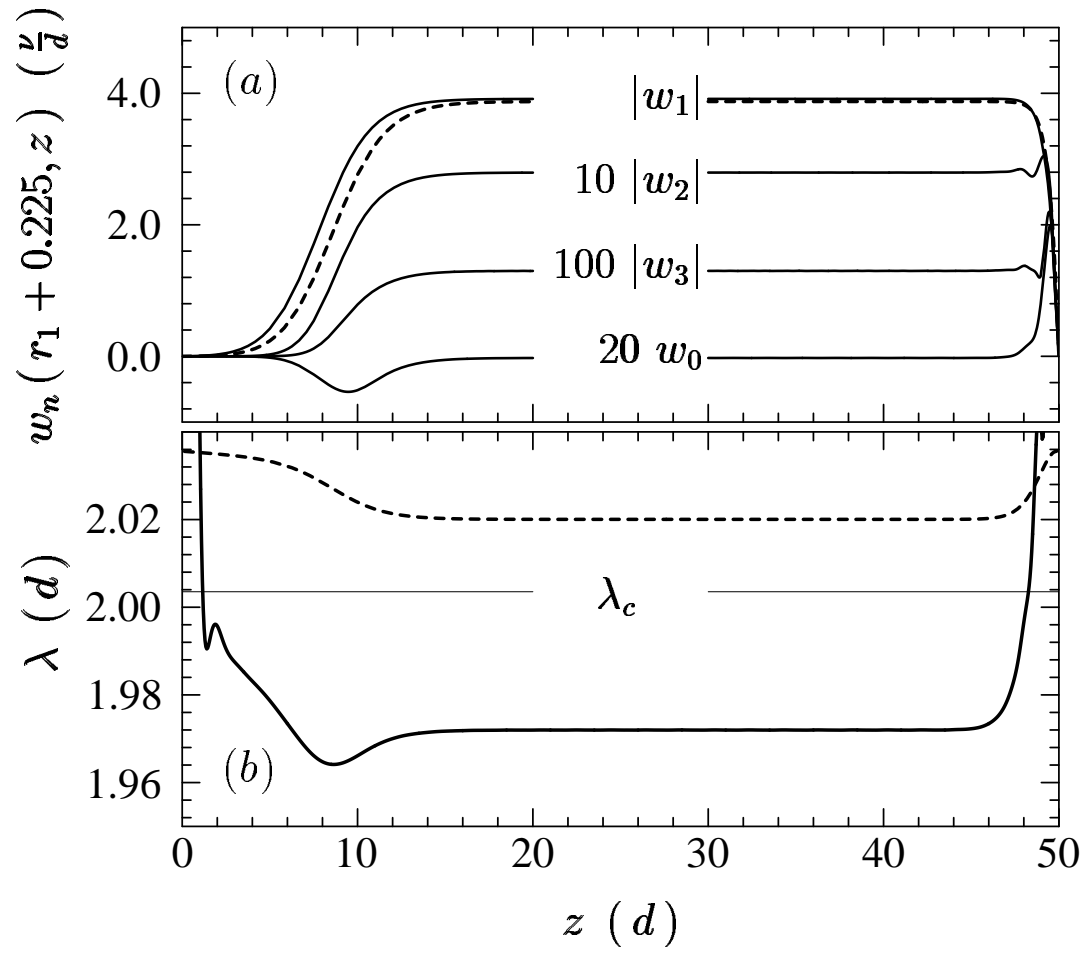


Figure 4
 Pattern selection in the absolutely unstable regime

P. Büchel et al., Phys. Rev. E

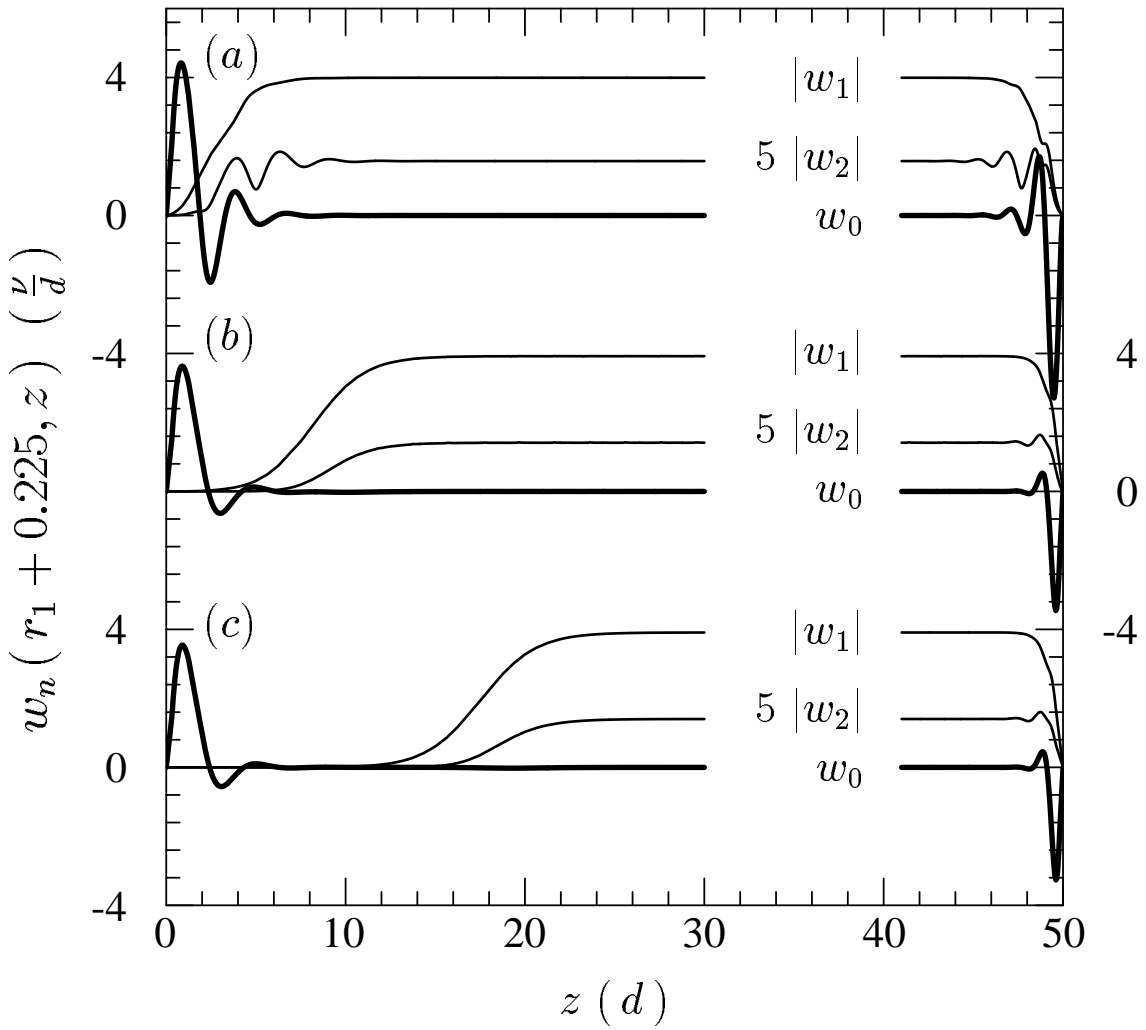


Figure 5
 Pattern selection in the absolutely unstable regime

P. Büchel et al., Phys. Rev. E

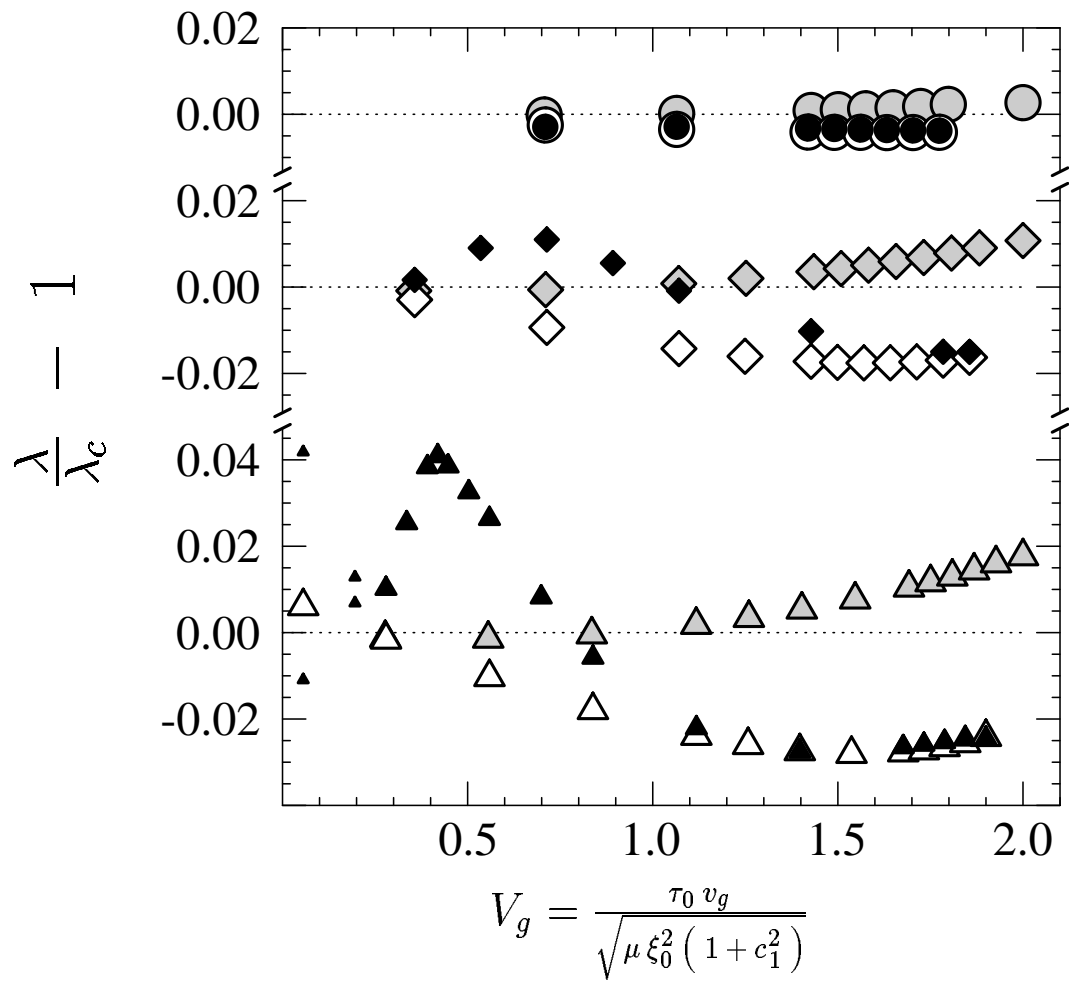


Figure 6
 Pattern selection in the absolutely unstable regime

P. Büchel et al., Phys. Rev. E

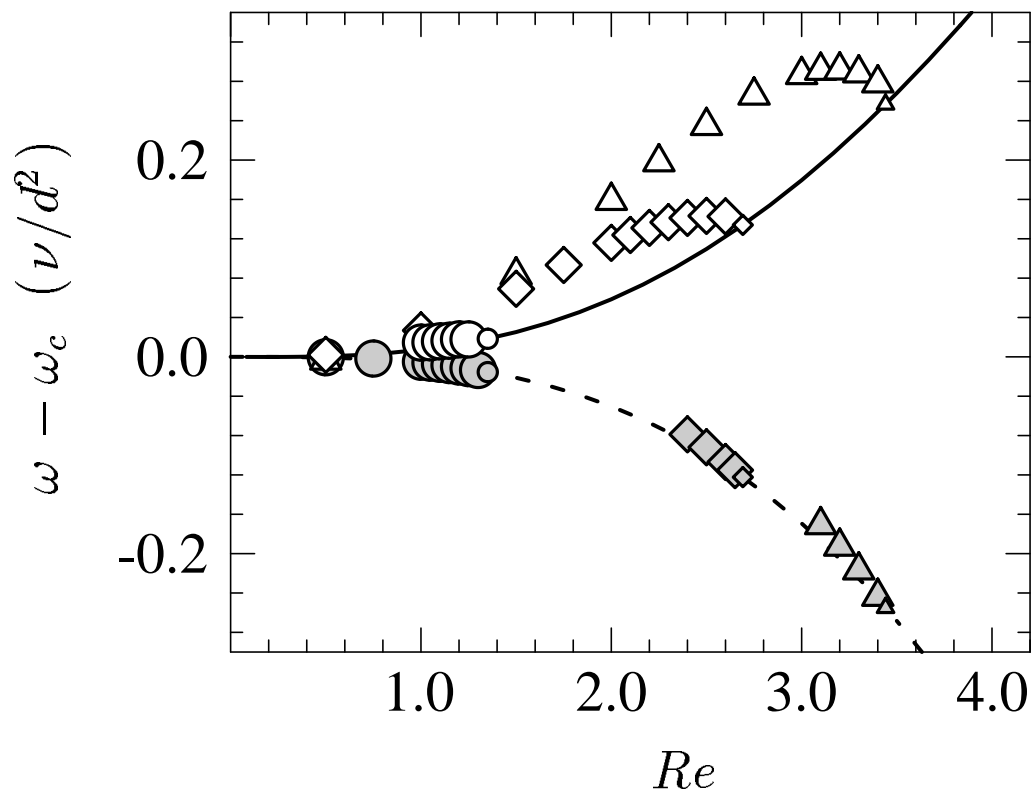


Figure 7

Pattern selection in the absolutely unstable regime

P. Büchel et al., Phys. Rev. E

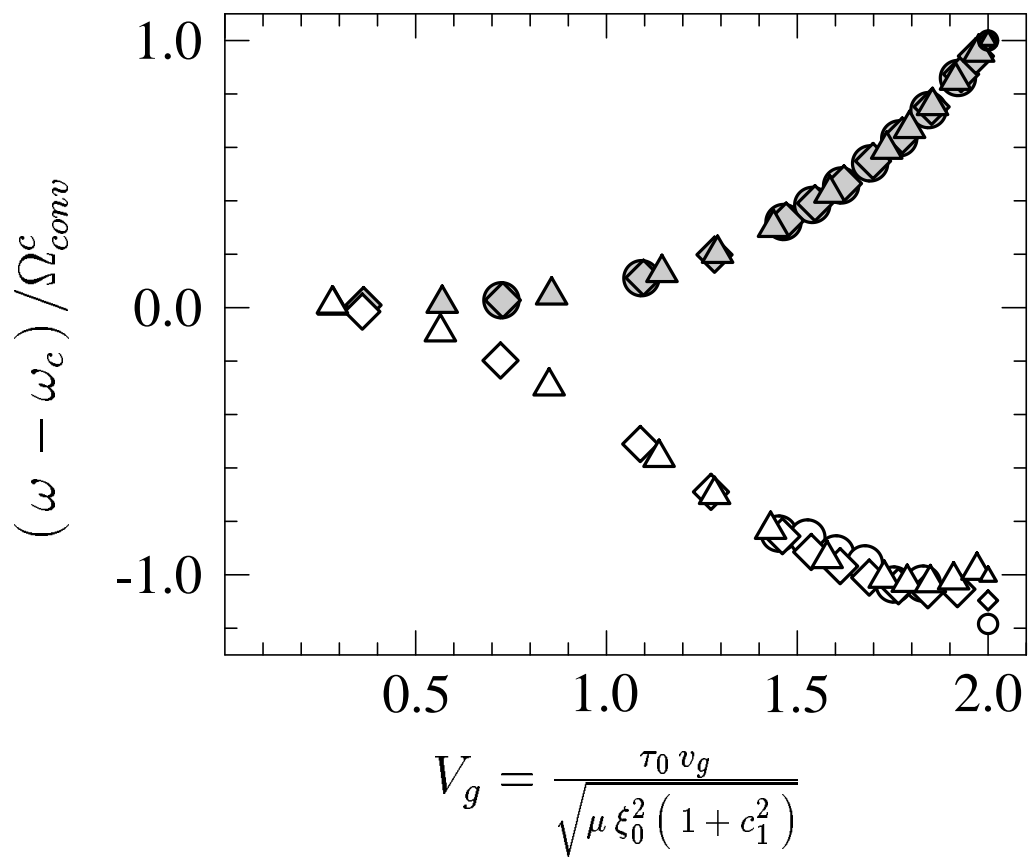


Figure 8

Pattern selection in the absolutely unstable regime

P. Büchel et al., Phys. Rev. E